RESEARCH

Heat transfer in Z-scan experiments

Rafal Miedzinski[1] · Izabela Fuks-Janczarek[1] · Luciana R. P. Kassab[2]

Abstract

In this study, we present the results of theoretical calculations concerning heat exchange in materials subjected to laser irradiation, with particular emphasis on Z-scan experiments. Using explicit difference methods, we model the temperature distribution in three-dimensional samples of various sizes, such as $[4 \times 4 \times 2]$ mm, $[5 \times 5 \times 2]$ mm, and $[6 \times 6 \times 2]$ mm. The simulations encompass two different types of pulsed lasers with durations of 10 (ns) and 100 (ps), adjusting laser parameters to achieve a peak irradiance intensity of 5 GW/cm^2. The temperature distribution in samples, denoted as $T(x, y, z, t)$, is computed using a novel laser heat source model specifically designed for this problem. The computational program Z-lambda enables not only the simulation of thermal processes during the Z-scan experiment but also post-experiment analysis. The development of this software was one of the main objectives of this study. The results indicate that the thermal analysis of Z-scan experiments requires consideration of factors such as laser pulse duration, laser repetition time, sample geometry, and heat exchange between the studied material and the surroundings. Especially in the Z-scan technique, controlling thermal parameters before the experiment is crucial for obtaining precise and reproducible results. It is noteworthy that sample heating during the experiment can significantly influence charge carrier density, subsequently affecting the parameters of nonlinear optics (NLO). Tools like the Z-lambda program allow for the optimization of laser parameters, minimizing sample heating, and reducing the thermal impact on NLO parameters.

1 Introduction

The complexity of the processes taking place during the interaction of the material with the laser radiation makes work on this topic a challenge for scientists both in experimental and theoretical fields. Therefore, the main goal of the research is not only to characterize and understand the basic processes of structural changes occurring in solids under the influence of strong radiation beams and use this knowledge to design optoelectronic devices, but also to calculate appropriate parameters, such as fluency thresholds and temperature distribution in the material as a function of time. This is important for applications, e.g. for optical elements for a new generation of radiation sources. In view of the above, scientists' research focuses not only on the analysis of the interaction between the material and the laser beam, but also on the related heat transfer from the laser to the material. Analytical and numerical models already exist in the scientific literature that focus on this process, allowing for a more complete understanding of both thermal and non-thermal procedures and the prediction of the outcome of these interactions [1–5].

There are also papers in the literature that present a transient temperature profile for a solid-state laser amplification system powered by a laser pump [6, 7]. Such generalized models can significantly affect the design process of laser systems and the prediction of window degradation in optical materials. In addition, the optical path description is directly applicable to thermal lens spectrometry, allowing correlation of the optical path change with the thermo-optical properties of solid materials.

In the case of a nonlinear optics experiment, especially in the context of the Z-scan technique, precise evaluation and

✉ Rafal Miedzinski
   r.miedzinski@ujd.edu.pl

   Izabela Fuks-Janczarek
   i.fuks@ujd.edu.pl

   Luciana R. P. Kassab
   kassablm@fatecsp.br

[1] Faculty of Science and Technology, Jan Dlugosz University in Czestochowa, Al. Armii Krajowej 13/15, 42200 Czestochowa, Poland

[2] Laboratório de Tecnologia em Materiais Fotônicos e Optoeletrônicos, Faculdade de Tecnologia de São Paulo, São Paulo 01124-060, Brazil

control of the thermal parameters of the sample prior to the experiment play a key role in achieving accurate and reproducible results. It is worth realizing that during a *Z*-scan experiment, when the sample is subjected to pulsed laser illumination, material heating can occur. This process can significantly affect the distribution of charge carrier densities, which in turn has a direct impact on the parameters of nonlinear optics (NLO). It should also be noted that the third-order nonlinear susceptibility is strongly dependent on temperature. An increase in temperature can lead to a change in the microscopic structure of the material, which affects the distributions of electron and photon energy densities, directly influencing the χ^3 value. Thanks to tools such as the *Z*-lambda program and the analyses performed with it, it is possible to determine the optimal laser parameters, such as pulse power, pulse frequency and pulse duration. Optimization of these parameters makes it possible to avoid excessive heating of the sample during the experiment and minimize thermal effects on the parameters of nonlinear optics.

However, the literature data show that analytical solving of heat transfer problems, with the exception of a few simplified cases, may be very difficult. In addition, analytical solutions are illustrative, but ineffective in many cases, presenting practical applications, especially in anisotropic materials and objects with complex configurations. Therefore, numerical methods are becoming more and more widespread, which is due to the very rapid increase in computational capabilities of modern computers, which now makes it possible to solve complex three-dimensional thermal research problems in a short time. Then, traditional numerical techniques such as finite difference (FDM), finite volume methods (FVM), finite element methods (FEM) and boundary element methods (BEM) are effective and repeatedly applied, and the development and application of new numerical methods represent important contribution in this area [8–12]. The numerical scheme based on the finite difference method is proposed in this article and has been used to analyze the heat propagation in solids under laser radiation. Such a procedure allowed to determine the temperature value at discrete spatial and temporal points. The three-dimensional model presented in the article was subjected to simulation of the heating process generated by the laser, followed by an analysis of the cooling process, taking into account both radiation and heat dissipation. Moreover the numerical procedures of the software are also discussed. The created program is a cross-platform tool that works on terminal of operating systems such as Linux, macOS and Windows. The article is organized as follows: Sect. 2.1 gives theoretical issues related to transverse electric and magnetic wave propagating in the free space, the law of heat conduction and information about applied numerical calculation. In particular, it is discussed in detail the finite differential element method for heat transfer and

introduced new absorptive profile function proper for applied calculations. Section 3.1 presents calculations and results. A case study on heat transfer characteristics in a sample subjected to intense nano- and pico-second laser irradiation is also presented here. In the Sect. 3.3, we delve into the thermal effects observed during the Z-scan experiment, focusing on PbOGeO$_2$ 2%Yb, 0.5%Tm, 1.0%Si material. Our analysis includes a detailed exploration of the heat transfer propagation dynamics within the tested materials, shedding light on the interplay between laser irradiation and thermal responses. Additionally, the section explores the influence of thermal conductivity at the thermocouple-material contact point on the overall temperature distribution within the sample. This section also verifies the accuracy of theoretical calculations performed using the *Z-lambda* software with experimental data. Conclusions are summarized in Sect. 4.

2 Theory

2.1 Transverse electric and magnetic wave propagating in the free space

Theoretical consideration will be based on the lowest-order transverse electric and magnetic (TEM$_{00}$) wave propagation in free space. The distribution of the electric field for the TEM$_{00}$ is described as follows [13, 14]:

$$E(x, y, z) = E_0 \left[\frac{\omega_0}{\omega(z)} \exp\left(-\frac{x^2 + y^2}{\omega^2(z)} \right) \right]$$
$$\times \exp\left[-j\left(k_\lambda z - \tan^{-1} \frac{z}{z_0} \right) \right] \quad (1)$$
$$\times \exp\left[-j\frac{k_\lambda(x^2 + y^2)}{2R(z)} \right]$$

The above equation consists the three factors. The first is related to the amplitude of the electric field while the beam propagates along the *z* axis. Amplitude of the electric field term is the function of the coordinates *x* and *y* which can be expressed by the radial coordinate given by $r^2 = x^2 + y^2$. The *j* is the imaginary unit. The equation below represents the laser beam radius along *z* coordinate:

$$\omega^2(z) = \omega_0^2 \left[1 + \left(\frac{\lambda_0 z}{\pi n \omega_0^2} \right)^2 \right] = \omega_0^2 \left[1 + \left(\frac{z}{z_0} \right)^2 \right] \quad (2)$$

where ω_0 is the beam waist, λ_0 is the wavelength and *n* is the refractive index. At the distance from the $z = 0$ point in the propagation direction the longitudinal and the radial phase factor change. The longitudinal phase factor is described by the second term of the equation while the radial phase

factor is expressed by the last term. Here $k_\lambda = 2\pi n/\lambda_0$ is the wavenumber and $R(z)$ is given by:

$$R(z) = z\left[1 + \left(\frac{\pi n \omega_0^2}{\lambda_0 z}\right)^2\right] = z\left[1 + \left(\frac{z_0}{z}\right)^2\right] \tag{3}$$

When considering thermal issues, it is convenient to derive the dependence of the spatial distribution of power (W/m^3) or energy (J/m^3) of laser light. Taking into account the linear and non-linear absorption of laser light, the energy transferred to the material can be calculated. On this basis the calculation of the temperature distribution $T(x, y, z, t)$ can be done. The Z-scan experiment uses both CW and pulsed lasers with specific radiation power and energy per pulse. Knowing the geometry of the laser beam and in particular the divergence angle, beam waist ω_0 and wavelength λ_0, we can obtain the irradiance I_0 for the focal point z_0. The electric field E_0 of such radiation at point z_0 can be calculated using the Poynting vector [15, 16]:

$$\mathbf{S} = \frac{c^2}{4\pi k_0}\mathbf{E} \times \mathbf{B} \tag{4}$$

in above equation the $\mathbf{B}$ is E/c and the time-averaged magnitude of the Poynting vector for a laser radiation is given by:

$$\overline{S} = \frac{c^2}{2\pi k_0}E\frac{E}{c} = \frac{c}{4\pi k_0}\overline{E}^2 \tag{5}$$

As $\overline{E}^2 = (1/2)E_0^2$, therefore the electric field E_0 is given by:

$$E_0 = \sqrt{\frac{8\pi k_0}{c}\overline{E}^2} \tag{6}$$

The total power crossing the plane xy along the z axis can be expressed by:

$$P = \frac{1}{2}\iint \frac{E_0^2}{\eta}dxdy \tag{7}$$

where $\eta = 376.7(\Omega)$ is the wave impedance of the plane waves for the free space. More precisely the wave impedance can be given as follows:

$$\eta = \sqrt{\frac{\mu_0}{\epsilon_0 \epsilon_r}} \tag{8}$$

where μ_0 is premeability constant and $\epsilon_0 = 1/(4\pi k_0)$ is the vacuum permittivity.

2.2 Z-scan experiment

Nonlinear optical properties play a crucial role in various applications, including laser technology, photonic devices, and material science. The Z-scan experiment offers a powerful means to characterize these properties, providing insights into how a material responds to varying light intensity. The schematic illustration of the apparatus was presented in the Fig. 1. The diagram depicts a laser emitting a Gaussian beam, denoted by the solid blue line. The experimental setup includes two photodetectors, PD1 and PD2, responsible for recording the intensity values I_0 and I, respectively. The system also comprises a sample, a beamsplitter (BS), an aperture (A), and a transmission plot.

This technique employs a focused Gaussian beam to assess the light transmittance of the examined sample. The sample's position is adjusted concerning the focal plane of a field lens, positioned at $z = 0$. The measurement is conducted away from the focus $(-z)$, where the transmittance remains relatively constant. Subsequently, the sample is displaced towards the focus and then to the position $+z$. In the case of a material exhibiting positive nonlinearity $(n_2 > 0)$, the $T(z)$ results initially depict a valley, followed by a peak. Conversely, for a sample with $n_2 < 0$, the results show the opposite pattern-first a peak and then a valley. During self-focusing phenomena, the beam becomes collimated by the sample, causing beam narrowing at the aperture and leading to an increase in the measured transmittance. Conversely, in the case of self-defocusing, the beam broadens at the aperture, resulting in a decrease in transmittance. The scanning process concludes when the transmittance returns to a linear behavior. Based on Eqs. (9) and 10 we can obtain the real and imaginary parts of the third order nonlinear optical susceptibility which can be expressed:

$$\chi_I^{<3>} = \left(\frac{\epsilon_0 c \lambda n_0^2}{3\pi}\right)\beta \tag{9}$$

$$\chi_R^{(3)} = 2\epsilon_0 c n_0^2 n_2 \tag{10}$$

where β is the two photon absorption, n_2 is the nonlinear refractive index—both values are obtained directly based on the Z-scan experiment, $\epsilon_0 = 8.85 \times 10^{-12}$ (F/m) represents electric permittivity, $c = 3 \times 10^8$ (m/s) is the speed of light, n_0 is the refractive index and λ is the wavelength. The role
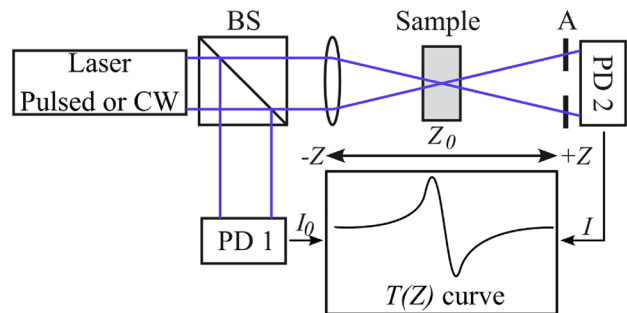

Fig. 1 Schematic representation of the Z-scan configuration

length of the sample in a Z-scan experiment is fundamental, as it directly affects measurement characteristics. We assume that the thickness has been precisely chosen, allowing us to neglect possible changes in the diameter of the laser beam inside the sample caused by diffraction or nonlinear refraction. In the context of linear diffraction, we assume that length of the sample $L << z_0$, while the criterion for nonlinear refraction assumes a material thickness $L << z_0/\Delta q_0$. The z_0 is the Rayleigh length defined by:

$$z_0 = \frac{\pi\omega_0^2}{\lambda} \tag{11}$$

where ω_0 is the laser's beam waist and λ is the laser's beam wavelength. In the scientific work dedicated to the theory of Z-scan as described by Mansoor Sheik-Bahae et al. [17], it was stated that the second criterion is satisfied when Δq is small. In the case of the first condition, based on experimental studies, a more restrictive condition $L < z_0$ was assumed. According to this assumption, the amplitude $\sqrt{I}$ and the phase q of the laser radiation as a function of z' are determined by the following pair of equations:

$$\frac{d\Delta q}{dz'} = \Delta n(I)k \tag{12}$$

$$\frac{dI}{dz'} = -\alpha(I)I \tag{13}$$

In these equations, $\alpha(I)$ determines the linear and nonlinear absorption conditions, and z' specifies the penetration depth of the sample by laser radiation. The β coefficient can be determined by finding a relation between the theoretical curve described by the equation below to the experimental results [16, 18]:

$$\Delta T(z) \approx -\frac{q_0}{2\sqrt{2}}\frac{1}{(1 + \frac{z^2}{z_0^2})} \tag{14}$$

In the equation above, q_0 and z_0 represents:

$$q_0 = \beta I_0 \frac{(1 - e^{-\alpha L})}{\alpha} = \beta I_0 L_{eff} \tag{15}$$

where q_0 is a parameter obtained by fitting the theoretical curve to the experimental scan, L is the sample length, and z_0 corresponds to the Rayleigh range. In the equations above, z represents the sample position with respect to the focal point. Negative values of z indicate that the sample is positioned between the focusing lens and the beam waist at focus, while positive values of z indicate that the sample is located between the focal point and the detector. The laser's beam waist radius is defined by ω_0, and the intensity of the incident beam at the focal point and the sample thickness are denoted respectively by I_0 and L. The transmission curve

obtained by scanning with the close aperture mode can be approximated as follows:

$$T(Z, \Delta q_0) \approx 1 - \frac{4x\Delta q_0}{(x^2 + 9)(x^2 + 1)} \tag{16}$$

In the above equation, $x = z/z_0$ and Δq_0 are the induced phase distortion of the laser Gaussian beam after being passed through the sample. When the curve described in Eq. (16) is symmetrical and possess the characteristic peak and valley, we can be calculate phase distortion Δq_0 the subsequent nonlinear refractive index n_2 using the equation below:

$$\Delta q_0 = \frac{\Delta T_{p-v}}{0.406(1 - S)^{0.25}} \tag{17}$$

$$n_2 = \frac{\lambda \Delta q}{2\pi I_0 L_{eff}} \tag{18}$$

where S is the fraction transmitted by the aperture.

2.3 The law of heat conduction

The thermal conductivity, is described by the Fourier law, which for the Cartesian coordinate system in a three-dimensional space can be expressed as follows [19–21]:

$$\begin{aligned}
\rho c_t \frac{\partial T}{\partial t} = & \frac{\partial}{\partial x}\left(\lambda_x \frac{\partial T}{\partial x}\right) \\
& + \frac{\partial}{\partial y}\left(\lambda_y \frac{\partial T}{\partial y}\right) \\
& + \frac{\partial}{\partial z}\left(\lambda_z \frac{\partial T}{\partial z}\right) \\
& + Q(x, y, z, t)
\end{aligned} \tag{19}$$

where T is the temperature (K), ρ is the material density (kg · m^{-3}), t is the time (s), λ_x, λ_y and λ_z are the thermal conductivity (W · m^{-1}·K^{-1}) in the orthogonal system with the following coordinates: x,y and z (m). The heat generation in the volume is expressed by the function $Q(x, y, z, t)$. In this paper, we consider a hexahedral sample that is heated by laser radiation. The heat accumulated in the sample will be released into the environment by radiative and convective heat losses which are expressed as follows [19, 22]:

$$-Q_r = \epsilon\sigma[T_A^4 - T_a^4] \tag{20}$$

$$-Q_c = h[T_A - T_a] \tag{21}$$

In both equations the T_A is the surface temperature (K) and the T_a is the ambient temperature. The coefficient ϵ in Eq. (20) represents the emissivity of the material and surface

type, σ is the Stefan–Boltzmann constant. In the Eq. (21), h is the heat transfer coefficient.

2.4 Volumetric heat model

To date, many models of laser heat sources $Q(x, y, z, t)$ have been developed for numerical simulations of heat distribution. In [23], the authors compared eight different models of other researchers for laser powder-bed fusion additive manufacturing. Models of laser heat sources normally take into account both the shape of the laser beam cross-section and the change in the intensity of laser light during material penetration. The heat model should contain all relevant factors that occur during a particular experimental case. In the Z-scan experiment, the laser light has a circular Gaussian distribution and the laser beam is only partially absorbed by the material [16, 24]. Therefore, the laser heat source model (LHSM) used in this paper will include the absorption, transmission and reflection coefficient of the material [25] and space geometry of the laser beam used for the Z-scan experiment. In the case of time-spatial geometry of the laser, the present model will describe a Gaussian laser beam for both continuous and pulsed light. Nevertheless, the calculations presented in the experimental section of this paper will use only pulsed lasers. The proposed three-dimensional model of the laser heat source used in Eq. (19) has the following form [23]:

$$Q(x, y, z, t) = \frac{2P(t)}{\pi \omega^2(z_c)} \exp\left(-2\left[\frac{x^2 + y^2}{\omega^2(z_c)}\right]\right) f(z_D) \qquad (22)$$

where $z_c = z - 1/2 S_L + z_D$—is the coordinate related to z position of the sample, S_L represents the sample's length position and the laser penetration depth is given by z_D. The $P(t)$ function has a Gaussian distribution with FWHM equal to the pulse duration. Finally the proposed absorptive profile function is given as follow [26]:

$$f(z_D) = \frac{\beta_{ht}}{S_L}\left[\frac{\left(1 - R_\lambda^2\right)}{T_\lambda}\right]^{-z_D/S_L} \qquad (23)$$

where β_{ht} is the effective thermal absorptivity of the laser light, R_λ and T_λ represent reflection coefficient and the light transmission of the material at laser wavelength λ, respectively.

2.5 Explicit difference method

Let's consider a hexahedral sample illuminated by laser light propagating along the Z axis. We assume that the sample's length S_L is less than z_0. The temperature distribution will be determined by the function $T(x, y, z, t)$. Calculations will be made using the explicit difference method. The dimension

of the sample are S_H, S_W and S_L and represent height, width and length respectively.

The sample is divided into control volumes, where the size of the single node is: $\Delta x = S_W/N$, $\Delta y = S_H/O$ and $\Delta z = S_L/P$. The N, O and P are the number of control nodes into which the sample was divided. The integer indexes i,j and k are related to the physical position of the node by the following dependencies $x = i \cdot \Delta x$, $y = j \cdot \Delta y$ and $z = k \cdot \Delta z$ where $i \in (-N/2, N/2)$, $j \in (-O/2, O/2)$ and $k \in (-N/2, N/2)$ respectively. The heat balance for three dimensional internal mesh can be expressed as follows [22, 27–29]:

$$c_t \rho \Delta x \Delta y \Delta z \frac{\mathrm{d}T_{i,j,k}}{\mathrm{d}t}$$
$$= \lambda \Delta y \Delta z \frac{T_{i-1,j,k} - T_{i,j,k}}{\Delta x} + \lambda \Delta y \Delta z \frac{T_{i+1,j,k} - T_{i,j,k}}{\Delta x}$$
$$\lambda \Delta x \Delta z \frac{T_{i,j-1,k} - T_{i,j,k}}{\Delta y} + \lambda \Delta x \Delta z \frac{T_{i,j+1,k} - T_{i,j,k}}{\Delta y} \qquad (24)$$
$$\lambda \Delta x \Delta y \frac{T_{i,j,k-1} - T_{i,j,k}}{\Delta z} + \lambda \Delta x \Delta y \frac{T_{i,j,k+1} - T_{i,j,k}}{\Delta z}$$

Approximating the derivative with the forward difference quotient, the temperature of a given node with indices i, j, k at the next time step $\tau + 1$ is as follows [29]:

$$T_{i,j,k}^{\tau+1} = T_{i,j,k}^\tau(1 - 2\xi_x - 2\xi_y - 2\xi_z)$$
$$+ \xi_x(T_{i-1,j,k}^\tau + T_{i+1,j,k}^\tau)$$
$$+ \xi_y(T_{i,j-1,k}^\tau + T_{i,j+1,k}^\tau) \qquad (25)$$
$$+ \xi_z(T_{i,j,k-1}^\tau + T_{i,j,k+1}^\tau)$$

where $\xi_x = a\Delta t/\Delta x^2$, $\xi_y = a\Delta t/\Delta y^2$ and $\xi_z = a\Delta t/\Delta y^2$ and $a = \lambda/\rho c_t$ (m²/s) is a temperature equalization coefficient. As we can see, the temperature of a node (i, j, k) located in a three-dimensional mesh at time $(\tau + 1)$ can be calculated from the temperature T^τ of neighboring nodes, where the integer τ is a time index related to time by the relation $t = \tau \Delta t$.

In the calculation the Robin boundary condition (third type boundary condition) are applied. Therefore, if the heat transfer is calculated for the nodes that are situated at the corner or at the wall of the samples, the heat balance have to take into account radiative and convective heat losses in accordance with Eqs. (20) and (21). The heat transfer of that nodes are more complicated and three separate equations should be evaluated for vertices, edges and faces. As we can see in the Fig. 2, those nodes are localized at six faces, twelve edges. For a better explanation, let the faces have the following names: front, back, left, right, upper and lower. Similarly the names of the edges will be upper-front, upper-back, upper-right, upper-left, left-front, left-back, right-front, right-back, lower-front, lower-back, lower-right

Fig. 2 The figure illustrates the distribution of selected nodes along the coordinate axes X, Y, Z in three-dimensional space. The example depicts a sample with dimensions $S_W = S_H = S_L = 1$ mm, divided into $N = O = P = 5$ nodes. Each individual node has dimensions $\Delta x = \Delta y = \Delta z = 0.2$ mm. Depending on the indices i, j, k indicating a particular node, its physical position in three-dimensional space can be precisely determined
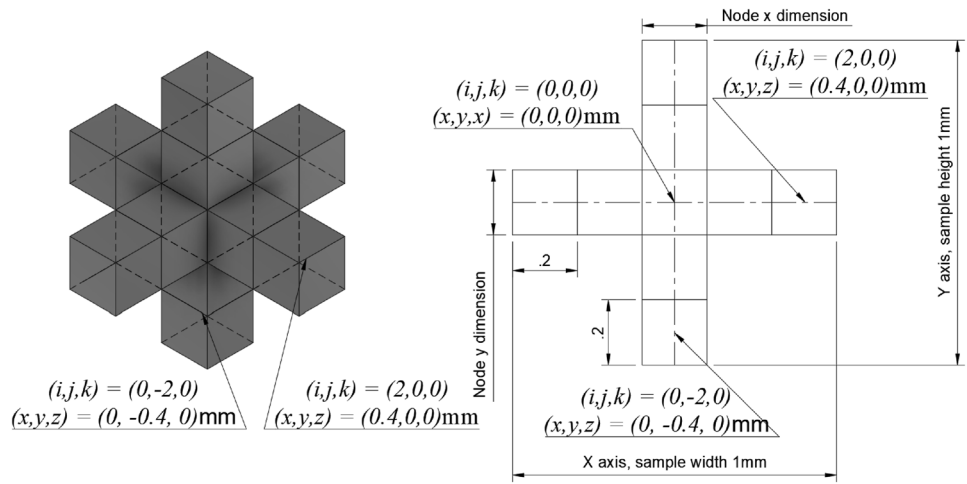
and lower-left. In addition of nodes localized at the faces and edges, there are the singles nodes localized at each vertices also. The heat balance for nodes located at the faces, specifically at the front face in this case, is as follows [29]:

$$
\begin{aligned}
c_t \rho \Delta x \Delta y \Delta z & \frac{dT_{i,j,k}}{dt} \\
= {} & \lambda \frac{\Delta z}{2} \Delta y \left(\frac{T_{i-1,j,k}^\tau - T_{i,j,k}^\tau}{\Delta x} + \frac{T_{i+1,j,k}^\tau - T_{i,j,k}^\tau}{\Delta x} \right) \\
& + \lambda \frac{\Delta z}{2} \Delta x \left(\frac{T_{i,j-1,k}^\tau - T_{i,j,k}^\tau}{\Delta y} + \frac{T_{i,j+1,k}^\tau - T_{i,j,k}^\tau}{\Delta y} \right) \\
& + \lambda \Delta x \Delta y \left(\frac{T_{i,j,k+1}^\tau - T_{i,j,k}^\tau}{\Delta z} \right) \\
& + \epsilon \sigma \Delta x \Delta y \left((T_A)^4 - \left(T_{i,j,k}^\tau \right)^4 \right) \\
& + h \Delta x \Delta y \left(T_A - T_{i,j,k}^\tau \right)
\end{aligned}
\tag{26}
$$

From the above equation, the temperature of a node located on the face at time $\tau + 1$ is calculated according to the following relationship:

$$
\begin{aligned}
T_{i,j,k}^{\tau+1} & \\
= {} & T_{i,j,k}^\tau (1 - 2\xi_x - 2\xi_y - 2\xi_z - 2\xi_z \zeta_{cf} - 2\xi_z \zeta_{rf} (T_{i,j,k}^\tau)^3) \\
& + 2\xi_z (T_{i,j,k+1}^\tau + \zeta_{cf} T_A + \zeta_{rf} (T_{Af})^4) \\
& + \xi_x (T_{i-1,j,k}^\tau + T_{i+1,j,k}^\tau) \\
& + \xi_y (T_{i,j-1,k}^\tau + T_{i,j+1,k}^\tau)
\end{aligned}
\tag{27}
$$

where $\zeta_{cf} = (h_f \Delta z)/\lambda$, $\zeta_{rf} = (\epsilon_f \sigma \Delta z)/\lambda$ and T_{Af} are the ambient temperatures in the front of the sample. The equations for the other faces have the same forms and they only differ by the coefficients related to geometry. The heat balance of nodes positioned at the edge should consider the ambient temperature, thermal conductivity, and emissivity of the two adjacent faces. This is crucial for thermal simulations to achieve greater accuracy. For instance, the samples are placed in the environment without a holder; however, the holder actually secures the sample with at least two bars. In this case, the thermal parameters differ from those at nodes surrounded by air. In Fig. 3, we observe that the node is positioned on the edge along the X axis, and two different faces are in contact with neighboring nodes, which is accounted for in the heat balance. In this scenario, these are the lower and front faces of the sample. The heat balance for the other eleven edges is similar and includes other thermal coefficients specified for the position of the considered edge. The temperature for the time step $\tau + 1$ of the node placed on the edge can be calculated as follows:

$$
\begin{aligned}
T_{i,j,k}^{\tau+1} & \\
= {} & T_{i,j,k}^\tau \left(1 - 2\xi_x - 2\xi_y - 2\xi_z \right) \\
& - 2T_{i,j,k}^\tau \left(\xi_y \zeta_{cy} + \xi_y \zeta_{ry} \left(T_{i,j,k}^\tau \right)^3 \right) \\
& - 2T_{i,j,k}^\tau \left(\xi_z \zeta_{cz} + \xi_z \zeta_{rz} \left(T_{i,j,k}^\tau \right)^3 \right) \\
& + 2\xi_x \left(T_{i-1,j,k}^\tau + T_{i+1,j,k}^\tau \right) \\
& + 2\xi_y \left(T_{i,j+1,k}^\tau + \zeta_{cy} T_{Ay} + \zeta_{ry} \left(T_{Ay} \right)^4 \right) \\
& + 2\xi_z \left(T_{i,j,k+1}^\tau + \zeta_{cz} T_{Az} + \zeta_{rz} \left(T_{Az} \right)^4 \right)
\end{aligned}
\tag{28}
$$

The coefficients presented in the equation above, ξ_x, ξ_y, and ξ_z, are the same as those introduced in Eq. (25). The ζ coefficients with subscripts c and r are associated with convective and radiative heat transfer, respectively. The subscript of ζ indicates the direction in which the nodes are in contact with heat transfer. Similarly, the subscripts of T refer to the

Fig. 3 3D model of the sample and its space coordinates. Left figure—bulk sample with heat maps on the faces, right figure—heat maps of the internal surfaces: $(x, y, 0)$, $(x, 0, z)$ and $(0, y, z)$
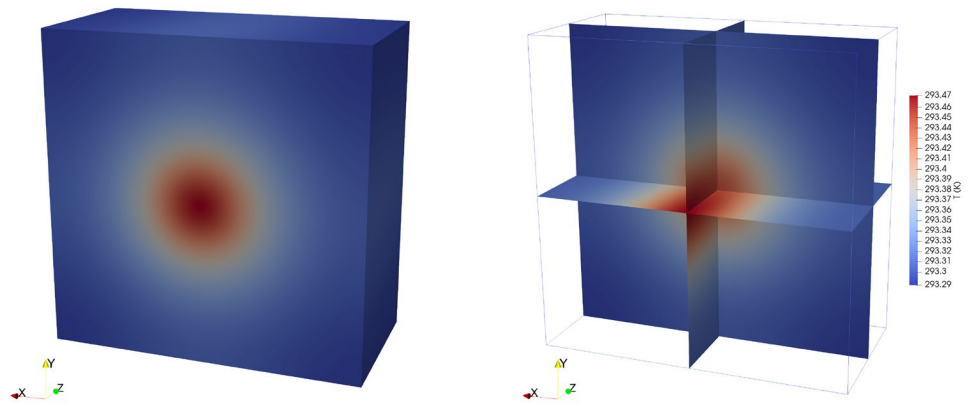
ambient temperature on the specific side of the sample. In the scenario described by Eq. (28), the nodes are in contact with the area on the front of the sample—along the Z axis $(\zeta_{cz}, \zeta_{rz}, T_{Az})$ and with the area on the lower face of the sample—along the Y axis $(\zeta_{cy}, \zeta_{ry}, T_{Ay})$.

As is shown in the Fig. 3, the node at the corner has three neighbors. Each vertex of the cubic sample is in contact with three areas. In most of the cases, the ambient temperature of the surrounding space is equal $T_{Ax} = T_{Ay} = T_{Az} = T_A$ such as the heat transfer coefficients $h_x = h_y = h_z = h$ and the emissivity coefficients $\epsilon_x = \epsilon_y = \epsilon_z = \epsilon$. But in some cases, applying all or some different coefficients will be necessary. For example polishing and/or dulling of the selected sample faces affect on the surface emissivity. Similarly, the sample mounting system also influences the aforementioned thermal coefficients. As previously mentioned, the temperature of the node belonging to the vertex is calculated according to the equation:

$$
\begin{aligned}
T_{i,j,k}^{\tau+1} &= T_{i,j,k}^{\tau}\left(1 - 2\xi_x - 2\xi_y - 2\xi_z\right) \\
&\quad - 2T_{i,j,k}^{\tau}\left(\xi_x\zeta_{cx} + \xi_x\zeta_{rx}\left(T_{i,j,k}^{\tau}\right)^3\right) \\
&\quad - 2T_{i,j,k}^{\tau}\left(\xi_y\zeta_{cy} + \xi_y\zeta_{ry}\left(T_{i,j,k}^{\tau}\right)^3\right) \\
&\quad - 2T_{i,j,k}^{\tau}\left(\xi_z\zeta_{cz} + \xi_z\zeta_{rz}\left(T_{i,j,k}^{\tau}\right)^3\right) \\
&\quad + 2\xi_x\left(T_{i+1,j,k}^{\tau} + \zeta_{cx}T_{Ax} + \zeta_{rx}\left(T_{Ax}\right)^4\right) \\
&\quad + 2\xi_y\left(T_{i,j+1,k}^{\tau} + \zeta_{cy}T_{Ay} + \zeta_{ry}\left(T_{Ay}\right)^4\right) \\
&\quad + 2\xi_z\left(T_{i,j,k+1}^{\tau} + \zeta_{cz}T_{Az} + \zeta_{rz}\left(T_{Az}\right)^4\right)
\end{aligned}
\tag{29}
$$

The temperatures at time step $\tau + 1$ are determined based on Eqs. (25), (27)–(29). The specific equation used depends on the node's position in the three-dimensional mesh. Internal nodes exchange heat with their neighbors, while outer nodes

additionally exchange heat with the surrounding environment. As previously demonstrated, the *z-lambda* software employs the aforementioned equations to compute the temperature of glass under the influence of laser light in the Z-scan experiment.

3 Results and discussion

3.1 Thermal effects with varying pulse durations

In this section of the paper, we will present the results of numerical calculations in which glass samples are exposed to lasers with pulse durations of 10 ns and 100 ps. The calculations simulate the conditions in which a hexahedral sample moves along the Z axis at a constant velocity v_s from the point $-z$ to the $+z$. In this area, the sample is illuminated by pulsed laser light with a frequency of f_r and pulse duration of τ. Depending on the position of the sample in the Z axis, the diameter of the laser beam changes according to Eq. (2). The beam waist is at $z = 0$ spot and the laser irradiance assumes the highest value of I_0. When the sample reach's the $+z$ point, the laser stops generating the pulses and the calculations are continued. During this time, the examined sample cools down and exchanges the heat previously gained by the laser to the environment. The calculations were made using the z-lambda software—which was specifically written for the purposes of the calculations presented in this article.

The software can be accessed at reference [30], while a comprehensive description of its utilization is delineated in the article denoted by reference [29]. The calculation were carried out for the glass samples whose physical parameters are presented in Table 1. The selected parameters of the examined materials are typical and are close to those of the wide group of tellurium glasses. The three glasses of various dimensions were selected for calculations [S_W x S_H x S_L]: [4 × 4 × 2] mm, [5 × 5 × 2] mm and [6 × 6 × 2] mm. The heat maps of the front faces depicting the heat

Table 1 Physical parameters of the sample and the environment assumed in calculations

Parameter	Unit	Value
Density	(kg/m^3)	2200
Specific heat capacity	(J · kg^{-1}· K^{-1})	745
Thermal conductivity	(W · m^{-1}·K^{-1})	1.38
Sample's initial temperature	(K)	298.150
Ambient temperature around the sample	(K)	298.150
The film coefficient boundary condition (all faces)	(W · m^{-2}·K^{-1})	5.0
Surface emissivity (all faces)	(1)	0.95
Light transmission at the used laser wavelength	(1)	0.55
Reflectance coefficient at the used laser wavelength	(1)	0.05
Sample's thermal laser beam absorptivity	(1)	0.25
Samples dimensions (W × H × D)	(mm)	4 × 4 × 2, 5 × 5 × 2, 6 × 6 × 2
Z-scan range—the distance between $-z$ and $+z$	(mm)	50
Sample's velocity	(mm · s^{-1})	1.0
Laser wavelength	(nm)	532
Beam radius at $z = 0$	(μm)	25.0
Beam irradiance at $z = 0$	(GW · cm^{-2})	5
Laser pulses repetition	(Hz)	10
Laser pulse duration 1	(ns)	10
Laser pulse energy 1	(J)	9.81748×10^{-4}
Laser pulse duration 2	(ps)	100
Laser pulse energy 2	(J)	9.81748×10^{-6}

induced in the sample by the first pulse at $z = -0.025$ (m) are illustrated in the Fig. 4. Parameters describing the $Z-$ scan experiment are summarized in the Table 1. Both lasers with short pulse durations were used in the analyses. All these lasers operated with a repetition frequency of $f_r = 10$ (Hz), and the pulse energy was selected so that the maximum power density at $z = 0$ was $I_0 = 5$ (GW/cm^2). Each of the three samples was exposed to nano- and pico-second laser beam. Fourier's law is a widely used principle in heat transfer theory that states that heat flow through a material is proportional to the temperature gradient. This law is based on the assumption of steady state heat transfer and thermal equilibrium in the material. When these conditions are met, the rate of heat transfer can be described using the Eq. (19). In the case of nanosecond and pico-second lasers, the heat transfer still occurs over a relatively short period of time, but may still have sufficient time to reach thermal equilibrium. Under such conditions, Fourier's law may be preserved and

Fig. 4 Heat maps of the examined samples [4 × 4 × 2, 5 × 5 × 2, 6 × 6 × 2] after the first pulse of the 100ps laser
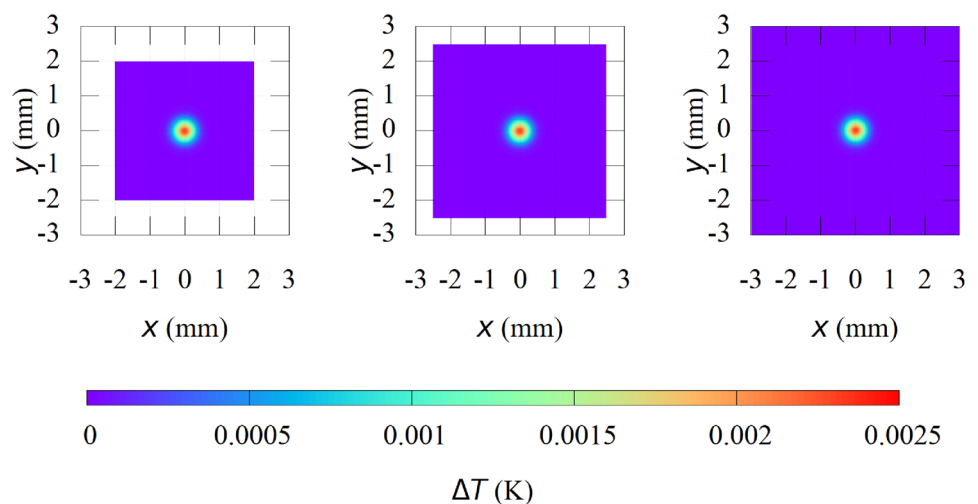
provide an accurate description of the heat transfer process. However, the applicability of Fourier's law in any given scenario depends on the specific conditions, such as the material properties, energy and duration of the laser pulse, and the temperature range involved. The sample's velocity during the Z-scan experiment was set to 1 (mm/s). Therefore, the Z-scan experiment was modeled for the first 50 (s), and the total simulation time of heat propagation in the sample was set to 180 (s).

The amount of heat accumulated by individual samples during the simulation is presented in Fig. 5.

The red line shows the amount of heat transferred to the material using a nanosecond laser, the green line refers to the simulations in which the pico-second laser was used. The shapes of all the curves are similar and at the first 50 s the heating of the samples is observed due to laser radiation. After this time we observe the cooling of the material attributed to the large spread of energy supplied to the samples by the individual lasers, and so the axis representing the value of the heat gained by the material was presented in Fig. 5 on a logarithmic scale. Different laser pulse energies had to be selected due to the previously assumed power density value of $I_0 = 5$ (GW/cm^2) for each different laser. In the case of the nanosecond laser, it had to be 0.982 (mJ) and for the pico-second laser 9.82 (μJ)—see Table 1.

Dependence of accumulated heat as a function of time for all modeled samples are presented in Fig. 6a, b. Solid, dashed and dotted lines refer to samples whose sizes are [4 × 4 × 2] mm, [5 × 5 × 2] mm and [6 × 6 × 2] mm, respectively. Additionally, these graphs expose areas that more accurately show the shape of the curves. These concerns the dependence of the accumulated heat during the first and
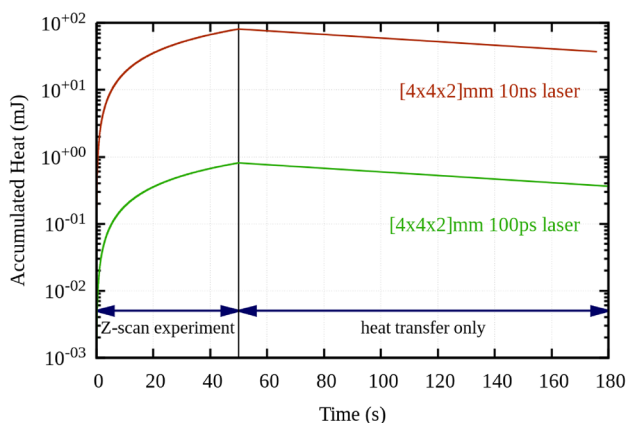
last second of laser operation in the Z-scan experiment. By analyzing these areas, we can see that thermal energy is delivered to the samples gradually. This means that with a laser pulse repetition frequency of 10 (Hz), ten steps are observed during 1 s. There is no significant difference in the amount of heat accumulated by the individual samples during the first second. These differences will be shown later. Fragments of the curve of stored energy at $t = 49.5$ (s) $+1.0$ (s) for the sample [4 × 4 × 2] mm shows that the absorption of the laser pulse is fast, while the release of heat energy to the surrounding is slow. This is related to the geometry of individual samples. The surface-area-to-volume ratio for a sample of [4 × 4 × 2] mm is 2.00, while for materials of [5 × 5 × 2] mm and [6 × 6 × 2] mm the ratio is 1.80 and 1.67, respectively. Therefore, taking into account the above-mentioned materials with a higher surface to volume ratio, heat in a shorter time is released. There may be a situation where, after the material is heated to a certain temperature and the energy transferred by the pulsed laser per unit time is appropriately determined (e.g. by changing the repetition of the laser pulses), the heat provided by the laser will be equivalent to the heat delivered by the tested material to the environment. On the enlarged parts of the graph showing the amount of accumulated heat at $t = 50$ (s) ± 0.5 (s) we see that the heat accumulated by the sample between the last and the penultimate laser pulse corresponds to the heat that the material delivers to the environment and corresponds to $5 \cdot t_r$, where t_r is the time between the laser pulses. In Fig. 3 the model of the sample in three-dimensional space is shown. The image on the right side of the 3D model shows the temperature maps of three perpendicular surfaces in the center of the sample and their position with respect to the coordinate system. These are $(x, y, 0)$, $(x, 0, z)$, $(0, y, z)$ surfaces.

These three surfaces are mutually perpendicular. For the modeled material with dimensions [4 × 4 × 2] mm, these surfaces are depicted in Fig. 7. This Figure shows the temperature distributions of the material at $t = 50$ (s), after the end of the laser exposure with a pulse duration of 10 (ns). During this time, the sample has moved away from the $-z$ to $+z$ point with a speed of 1 (mm/s) covering a distance of 50 (mm). At that time, the sample was exposed to laser pulses. By analyzing surface temperature distributions, it is possible to determine the temperature change along individual coordinate axes (X, Y, Z). Temperature distribution on surface $T(x, y, 0)$ is symmetrical. Therefore the dependence on $T(x, 0, 0)$ and $T(y, 0, 0)$ is the same. The Fig. 8a, b show dependence on $T(x, 0, 0)$, $T(y, 0, 0)$ and $T(z, 0, 0)$ for $t = 50$ (s) $+\Delta t$. Here the Δt time were: 100 (ms), 200 (ms), 300 (ms), 400 (ms), 500 (ms) and 1000 (ms). The analysis of the temperature distribution inside the material shows that the sample with dimensions [4 × 4 × 2] mm warms up to higher temperatures than those with dimensions of [5 × 5 × 2] mm

Fig. 5 Thermal energy of the samples transferred by laser radiation. The applied color scheme of individual curves is: red—ns laser and green—ps laser. Diagram showing the dependence of the thermal energy transferred to the samples by the laser radiation as a function of time. The curves in the diagram are indicated using the following color scheme: red for laser ns and green for laser ps

Fig. 6 Thermal energy of the samples irradiated by 10 ns (**a**) and 100 ps (**b**) pulses of laser radiation

(a)

(b)
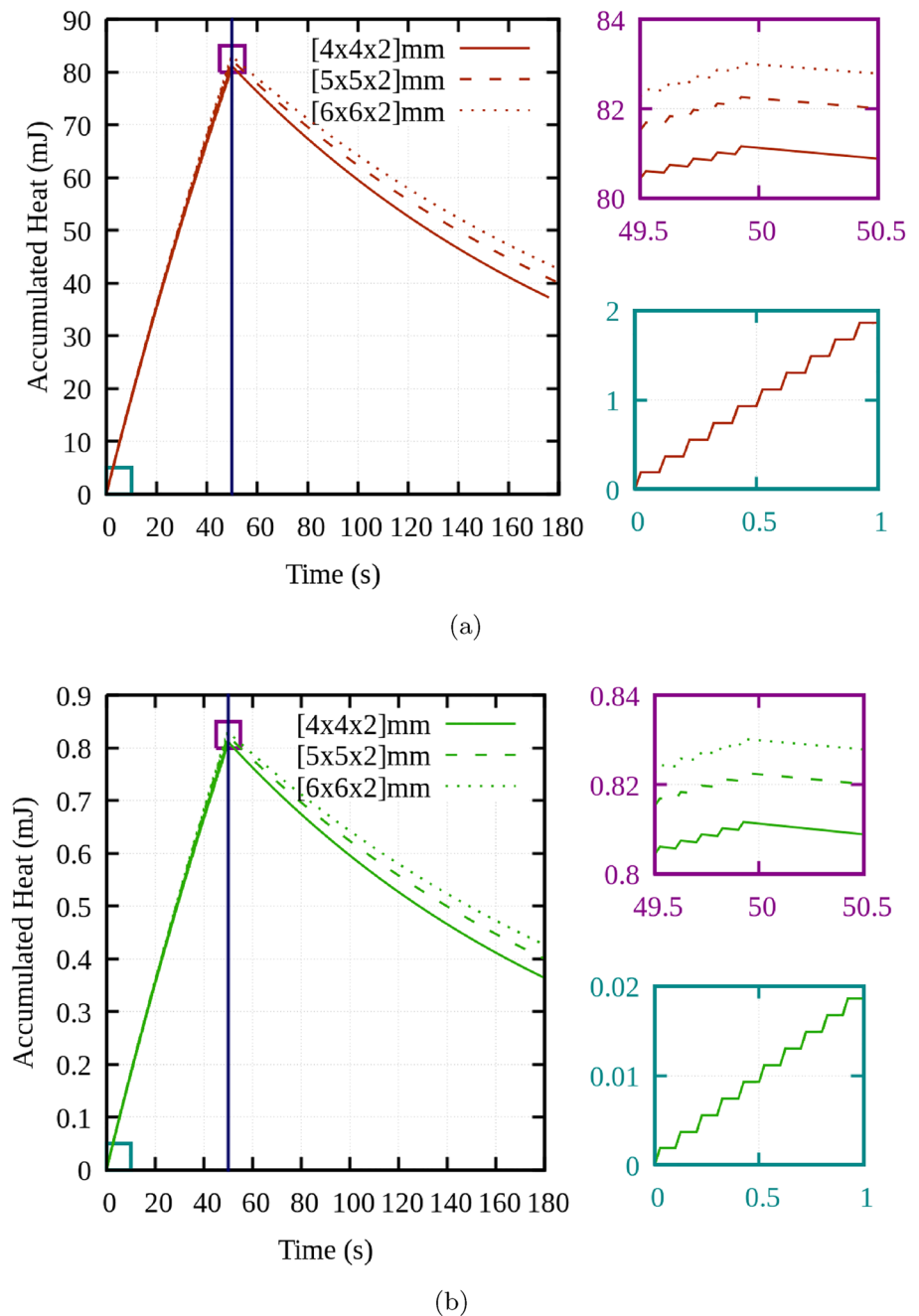
and [6 × 6 × 2] mm. This was clearly shown by the results of the numerical simulations for all the two different lasers used. Obviously, the increase in temperature of the tested material is greater for lasers whose pulse duration is longer. The reason for this is that the laser energy with a longer pulse duration is greater. This allows to keep the power density assumed in the simulation at the $z = 0$ point equal to $I_0 = 5 \, (\text{GW} \cdot \text{cm}^{-2})$. Interestingly, after one second without laser radiation, the sample's center temperature with size of [4 × 4 × 2] mm decreases slower with respect to larger materials. In the case of glasses irradiated with a nanosecond

laser, the temperatures at (0, 0, 0) point decreased after $\Delta t = 1000 \, (\text{ms})$ by $\Delta T = 0.1481 \, (\text{K})$, $\Delta T = 0.1564 \, (\text{K})$ and $\Delta T = 0.1614 \, (\text{K})$ for glasses with sizes of [4 × 4 × 2] mm, [5 × 5 × 2] mm and [6 × 6 × 2] mm, respectively. Despite the higher temperatures inside [4 × 4 × 2] mm sample, the thermal energy stored in the entire volume is smaller. A very important parameter determining the heat exchange with the environment is the relation between the surface size of the tested material to its volume. All modeled materials analyzed in this article have thickness of 2 (mm), while the width and height of these materials vary. As it results from
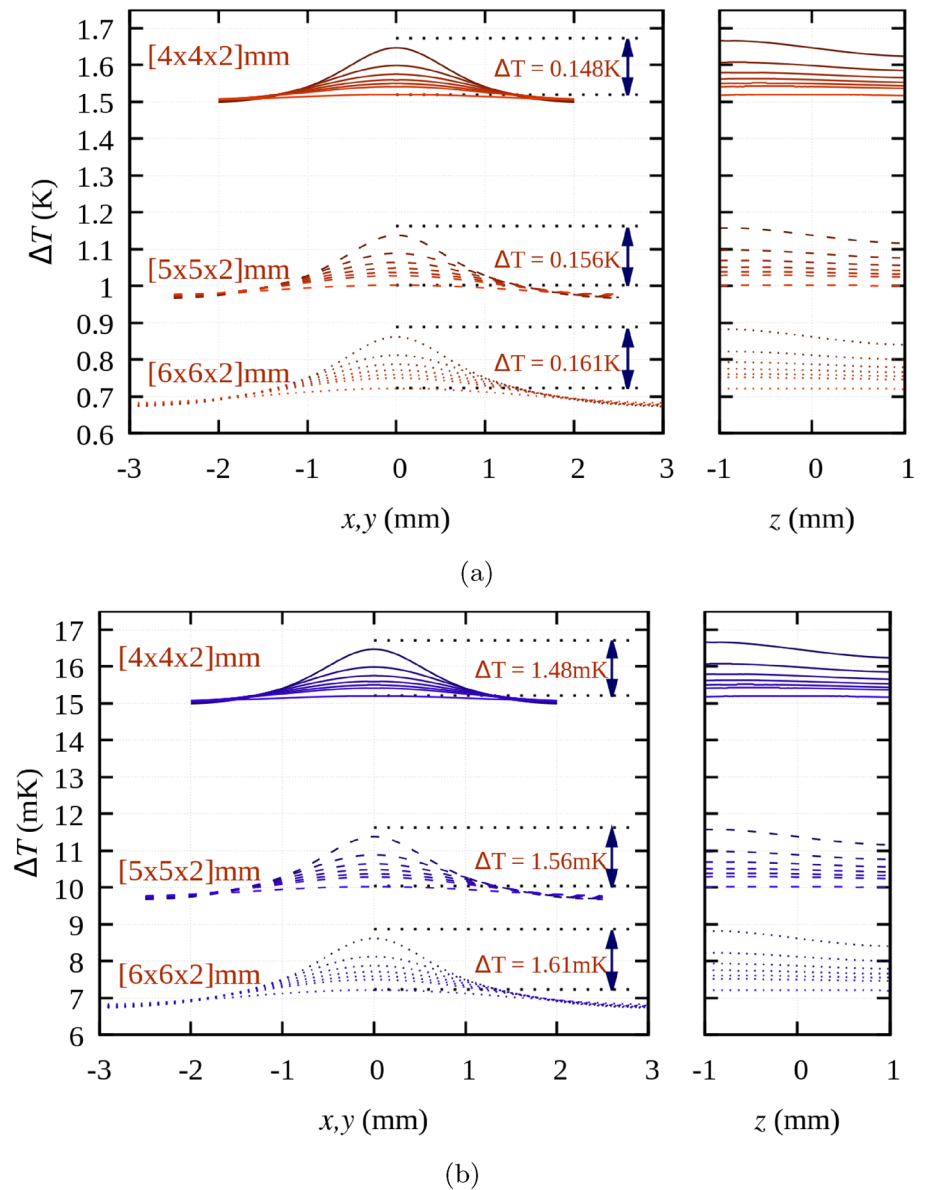
Fig. 7 Internal heat maps of the $[4 \times 4 \times 2]$ mm sample for time $t = 1.000$ s treated by 10 ns pulse duration laser
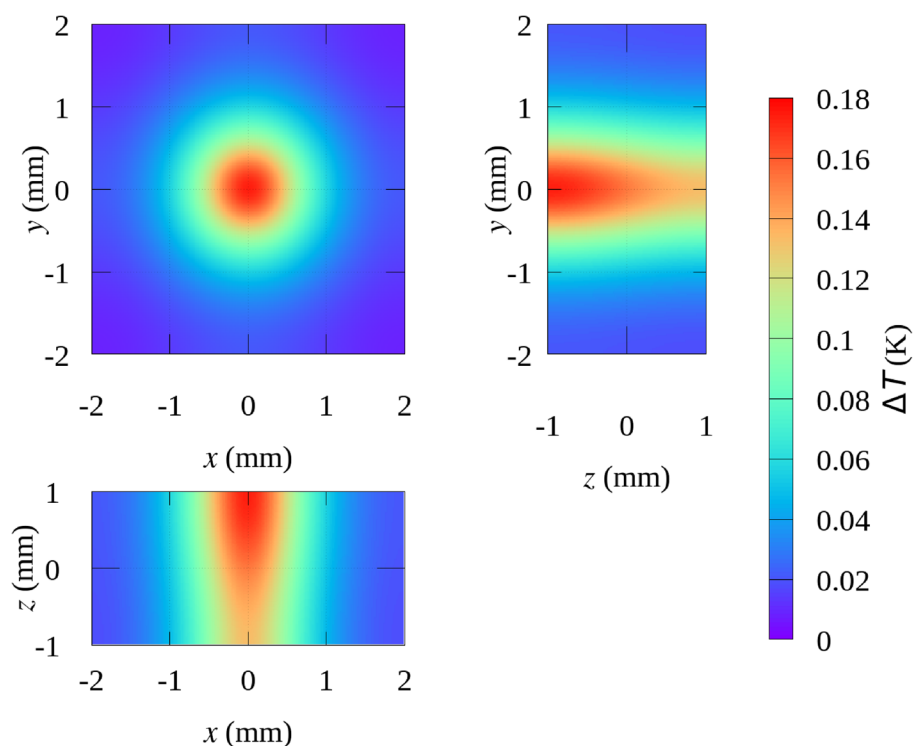
the presented calculations, the geometry of the material strongly influences the distribution and propagation of heat of the tested material. In the materials studied, the values of the surface-to-volume ratio (S_A/V) are higher for materials with smaller heights and widths. This has a direct impact on the heat exchange with the environment. The sample with the smallest size of $[4 \times 4 \times 2]$ mm gives off heat faster, although it is heated to a higher temperature than the samples with larger sizes. It should also be noted that all samples, regardless the size, receive the same amount of heat from the laser. Therefore, the quotient of the absorbed thermal energy of a given sample and the volume is the largest for the smallest sample. This situation is illustrated in Fig. 9. We can see the temperature distribution for the (0, y, z) planes for all the three modeled samples. Analyzing the temperature maps starting from the left, we can see the results after irradiation with the first nanosecond laser pulse. The following figures show the temperature distribution at 2.5 (s), 5.0 (s), 7.5 (s) and 10.0 (s). We can clearly see that the temperature in the central part of the $[4 \times 4 \times 2]$ mm sample, after 10 (s) from the start of the experiment, increased by about 0.5 (K), and the temperature of the outer parts increased by more than 0.3 (K) from $t = 0$ (s). The changes of the temperature for $[5 \times 5 \times 2]$ mm and $[6 \times 6 \times 2]$ mm samples are definitely smaller. The central part of the sample $[5 \times 5 \times 2]$ mm treated by 10(ns) pulse duration laser was heated by about 0.35 (K) and the $[6 \times 6 \times 2]$ mm sample by about 0.3 (K). It can also be observed that the outer parts of these samples are cooler than $[4 \times 4 \times 2]$ mm sample. A similar temperature

distribution is observed when the samples are illuminated with pico-second (Fig. 8b) laser. The temperature changes are of the order of (mK). It should be mentioned that the volumes of the samples of the present study are 32, 50 and 72 (mm^3). Therefore, the smallest volume sample heats up to highest temperatures. This is due to the fact that the smallest volume sample receives a greater amount of energy per unit volume from a single laser pulse. At the same time, the glass with the smallest size delivers more heat to the environment, which is related to the S_A/V ratio. The Fig. 10 presents additional results related to the heat gained by the material under nanosecond laser excitation. In this case the $[4 \times 4 \times 2]$ mm sample was used in the numerical simulation. The sample was illuminated with a nanosecond laser with a repetition frequency of 10, 20, 40, 60, 80 and 100 (Hz). The other physical parameters used for the numerical calculations were the same as those used in the previous calculations of this section. In these calculations, the amount of heat supplied to the sample was adjusted by changing the laser repetition frequency. On the enlarged fragment of the Fig. 10 a strong correlation can be seen between the amount of heat accumulated in the sample and the frequency or type of laser used. The known fact is that lasers with shorter pulse duration do not cause such strong thermal phenomena as continuous lasers or pulsed lasers with long pulse duration, e.g. of the order of (μs). Moreover, during the examination of the materials, especially in the Z-scan experiment, where the one single spot of the sample is exposed, an important factor that influences heat transfer is not only the pulse duration,

Fig. 8 The temperature of the sample in time $t = 50$ s $+\Delta t$ where $\Delta t = 100, 200, 300, 400, 500$ and 1000 ms for time duration of lasers 10 ns (**a**) and 100 ps (**b**)

3.2 Thermal effect for the sample with different surface to volume ratio

In this section, we present the thermal effects observed in samples with distinct surface-to-volume ratios during the Z-scan experiment, where they are exposed to pulsed laser irradiation. The calculations provide insights into how varying surface-to-volume ratios influence the thermal response of the samples. The presented graph in Fig. 11a visually depicts the theoretical correlation between cumulative energy and scan duration, computed using the Z-lambda software. The accompanying subfigure table offers additional details on sample dimensions and their respective surface-to-volume ratios. The surface-to-volume ratio is an important parameter that affects the efficiency of heat transfer, which can have important consequences for the thermal properties of the materials under study. One can visually observe dynamic fluctuations in the value of accumulated energy during the 150-second scanning experiment along the z-axis. Note that the value of cumulative energy increases in the initial period from 0 s to 20 s. During this time, the sample absorbs and stores heat, which is delivered in the form of a laser pulse. In the next 20 s, there is a process of heat dissipation by the sample to the environment. The process of heat dissipation by the sample to the environment is correlated with convection and radiation, represented by
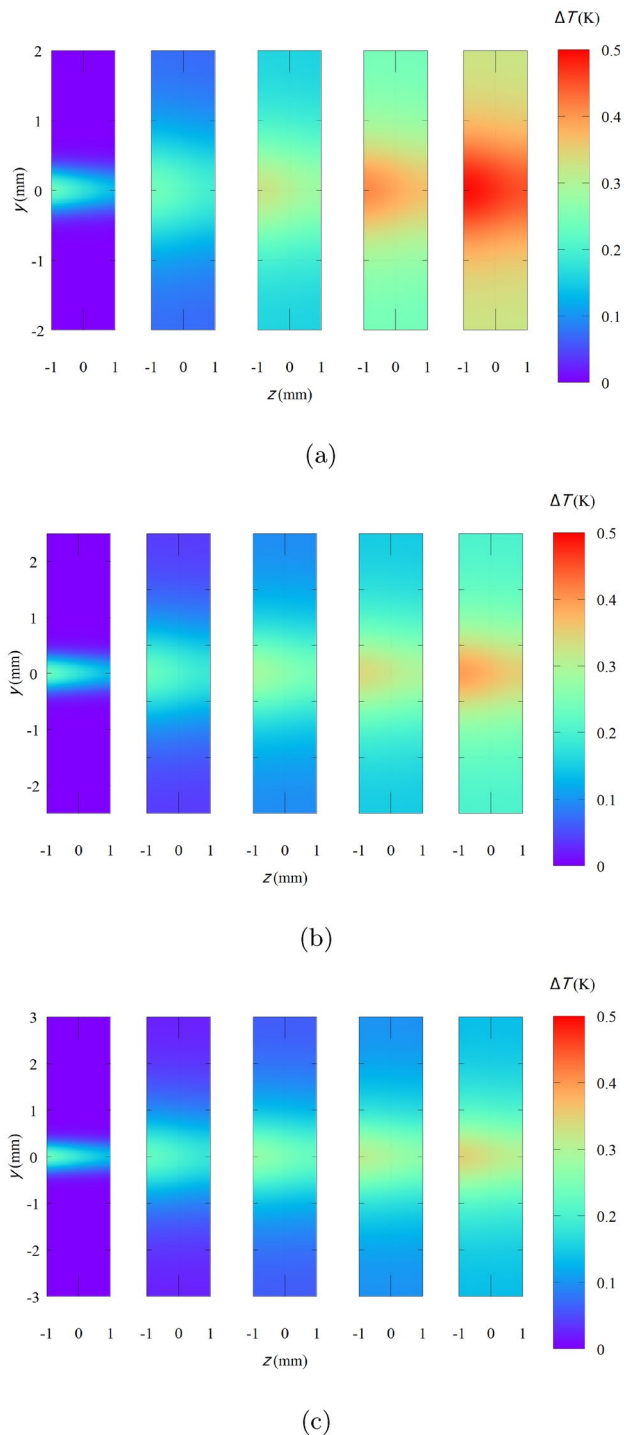
but also the material geometry, the ratio of surface area to volume, frequency laser repetition, the exposure spot of sample, or the divergence of the laser beam.

(a)

(b)

(c)

Fig. 9 Internal heat maps of the samples with dimension of [4 × 4 × 2] mm (**a**), [5 × 5 × 2] mm (**b**) and [6 × 6 × 2] mm (**c**) irradiated by 10 ns pulsed laser in time: 2.5 s, 5.0 s, 7.5 s, 10.0 s

Eqs. (20) and (21). Heat is dissipated most efficiently by the sample with the smallest size, which is related to the larger contact area with the environment. For small samples, the volume-to-area ratio is greater than in larger samples. Since

thermal conduction mainly occurs through the surface, a smaller sample with a larger surface-to-volume ratio is able to efficiently dissipate heat to the environment. Describing the situation between the 55th and 85th seconds of 11b, there is a sharp increase in the accumulated heat in the sample. This increase can be attributed to several factors, and the key aspect is the diameter of the laser beam. During this period of time, the diameter of the laser beam tends to the minimum (ω_0), which means that the size of the area where the laser energy is focused is the smallest. At the same time, it is said to reach the maximum energy density in a pulse. This means that despite the reduction in beam size, intensity of each pulse is at its peak. A laser beam with a smaller diameter concentrates more energy in one area, which can lead to intense heating of the sample material. The laser's energy density, reaching a maximum, can cause local heating of the sample, which in turn results in a sharp increase in accumulated heat.

Figure 12 presents the theoretical temperature distribution for samples differing in the size of the surface on which the laser pulses fall. Figure 12a illustrates the morphology of the sample surface after the first laser pulse is applied. Regardless of the size of the sample, the first pulse has a constant diameter, and the temperature distribution inside the sample is about 0.4 K in the center and decreases, reaching a value of about 0.1 K at the edges. After a few milliseconds, before the second laser pulse arrives, the heat provided by the first pulse dissipates into the sample. For the sample with the smallest size (Fig. 12b), the heat quickly reaches the edges, where further cooling occurs. In contrast, for samples having larger sizes at the same time, there are areas at the edges where the heat has not reached, keeping their temperature at about 0.0002 K. Theoretical data shows that by the time the second pulse reaches the center of the sample, its temperature will have dropped significantly to about 0.0014 K.

3.3 Verification of the applied numerical method

In our previous report [31], we demonstrated that $PbOGeO_2$ glasses with Si nanoparticles can be effectively used to construct optical devices operating at 532 nm. However, the effect of temperature on Z scanning experiments was not studied in that paper, unlike the one discussed in this article. In order to verify the theoretical model proposed in this article, it was decided to conduct additional research related to heat propagation in the sample using a z-scan experiment. A material consisting of $PbOGeO_2$ doped with 2%Yb, 0.5%Tm, 1.0%Si, with dimensions of 4.95 (mm) × 6.40 (mm) × 2.60 (mm), was selected as the sample. The sample was placed in the holder shown in the Fig. 13. The figure illustrates the placement of the sample in a holder whose lower and upper edges terminate in a thermal insulator. The thermocouple was precisely placed in the center of the lower

Fig. 10 The heat collected by [4 × 4 × 2] mm sample treated by 10ns laser with pulse repetition 20, 40, 60, 80 and 100 (Hz)
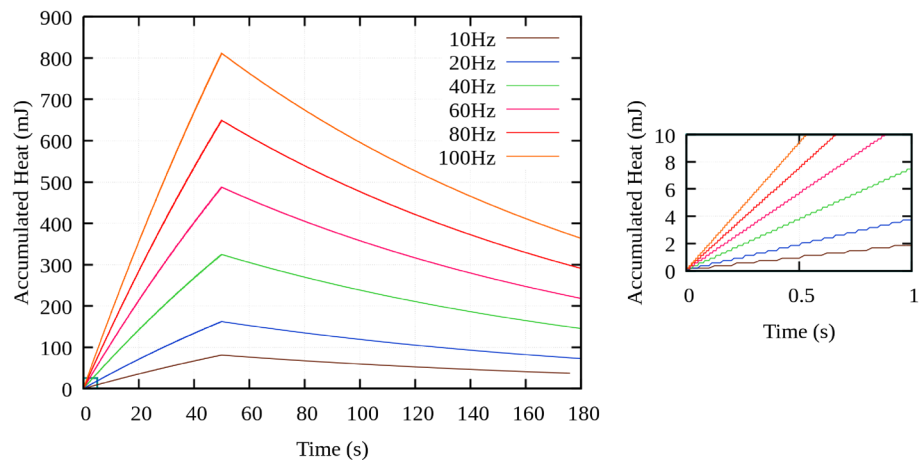
surface of the sample, between the insulator and the center of that surface. The other four surfaces were not thermally insulated and were in direct contact with the environment. In the context of the Z-scan experiment being conducted, the temperature measurement process was accomplished by placing the entire holder along with the sample and thermocouple in a specially prepared thermal chamber. This procedure was aimed at obtaining an accurate measurement of the temperature of the test sample, isolating it from external influences and ensuring stable thermal conditions.

The temperature was read using a 24-bit ADC, which guaranteed high accuracy and resolution of the measurement. The process of exposing the sample during the Z-scan experiment lasted 120 s, after which the temperature of the lower surface of the sample continued to be monitored for another 180 s. As a result, the temperature of the lower surface of the sample was recorded for 300 s. The results obtained were the main parameters used in the theoretical calculations. Within the framework of the conducted tests, a laser with a wavelength of 532 nm was used. The repetition rate of laser pulses was set at 10 Hz, while the duration of a single pulse was 5 ns. The sample was moved along the Z-axis in the range of $-25 \leq z_0 \leq +25$ mm. The penetration depth, defines the distance within the material at which the incident light intensity is attenuated to $1/e$ of its initial value. Considering the absorption of laser light by the glass and its thickness, the laser beam penetrates the material throughout its thickness. This is evident in Fig. 9, which shows temperature distributions along the direction of laser light transmission. If the material had higher absorption, the beam would heat the material superficially. A extreme case of such an effect is laser ablation, which involves removing part of the material using a laser beam. In the case of the Z-scan experiment, it is essential to first ensure the appropriate selection of the material thickness L with respect to the Rayleigh length. With the assumed laser beam geometry, the Rayleigh length is $z_0 = 8.1$ mm, so the condition $L < z_0$ for samples of

$L = 2.60$ is satisfied. The second crucial factor is to ensure the proper transmission of light through the material so that the laser light does not damage the sample due to excessive absorption. The total duration of scanning in this range was 120 s, which made it possible to determine the speed of movement of the sample along the Z axis as $v_z = 0.4167$ (mm/s). The validity of the theoretical calculation was evaluated by comparing the experimental and theoretical temperatures at the central point of the bottom surface of the sample. As shown in Fig. 14, the sample rapidly absorbs heat in the first 60 s of laser radiation. Subsequent heat accumulation continues, although the rate of this process decreases due to heat losses associated with radiation and convection. These heat losses are particularly noticeable after 120 s, the end of the laser. At this point, there is a sharp drop in the thermal energy of the sample. Figure 14 indicating concurrence between experimental and theoretical results.

According to theoretical calculations, the maximum temperature increase was 0.066 K, while in the case of the experiment, the temperature reached 0.055 K. In both cases, the maximum temperature was recorded after 120 s, that is, after the laser was turned off. After this time, as expected, a decrease in temperature was observed, resulting from the natural cooling of the sample to ambient temperature.

It is important to emphasize a significant element of the theoretical analysis, i.e. the parameter related to the point of contact between the thermocouple and the material surface, which determines the higher thermal conductivity in this area. The metal thermocouple draws heat from the material more efficiently than other areas of the sample. This aspect was taken into account in the calculations, and the Fig. 15 shows the results of this assumption. This image shows the temperature distribution in the $(X, 0, Z)$ plane of the sample for 10, 30, 50, 70 and 90 s. It can be seen that the thermally isolated upper part of the sample, due to its contact with the thermocouple, is cooler than

Fig. 11 **a** Present plots the theoretical relationship between cumulative energy and the time duration of a Z-scan experiment for samples with different surface-to-volume ratios. They show the dynamic changes in the value of accumulated energy in the samples during a 150-second scanning experiment along the z-axis. **b** Illustrates the moment when the samples were in the laser focus region during the Z-scan experiment
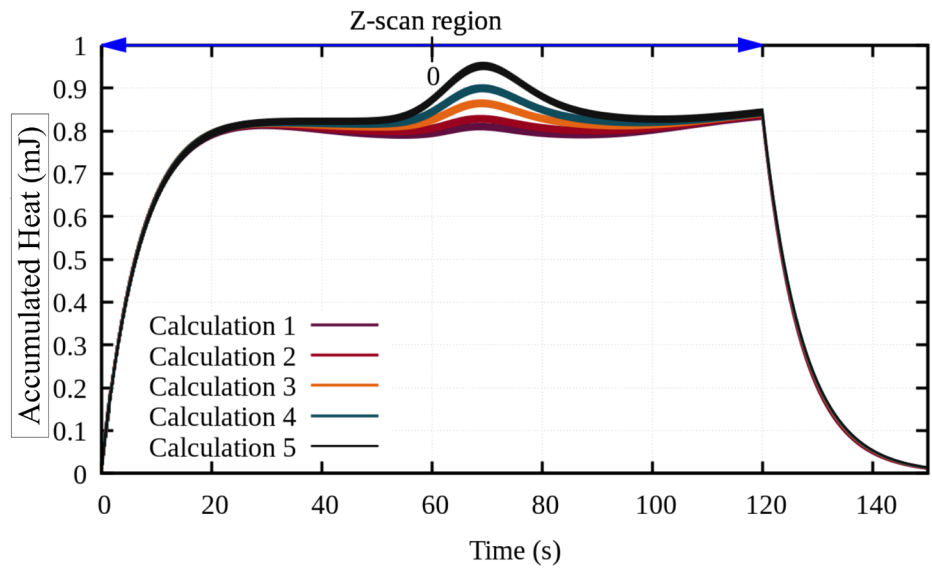
Dimensions of the samples with differ surface to volume ratio, used during the numerical calculations.

Name	x (mm)	y (mm)	z (mm)	Surface to Volume ratio (mm^{-1})
Calculation 1	4.50			1.81
Calculation 2	4.90			1.77
Calculation 3	5.50	4.90	2.10	1.73
Calculation 4	5.90			1.70
Calculation 5	6.50			1.67

(a)

(b)

(a)

(b)

(c)

(d)

(e)

(f)
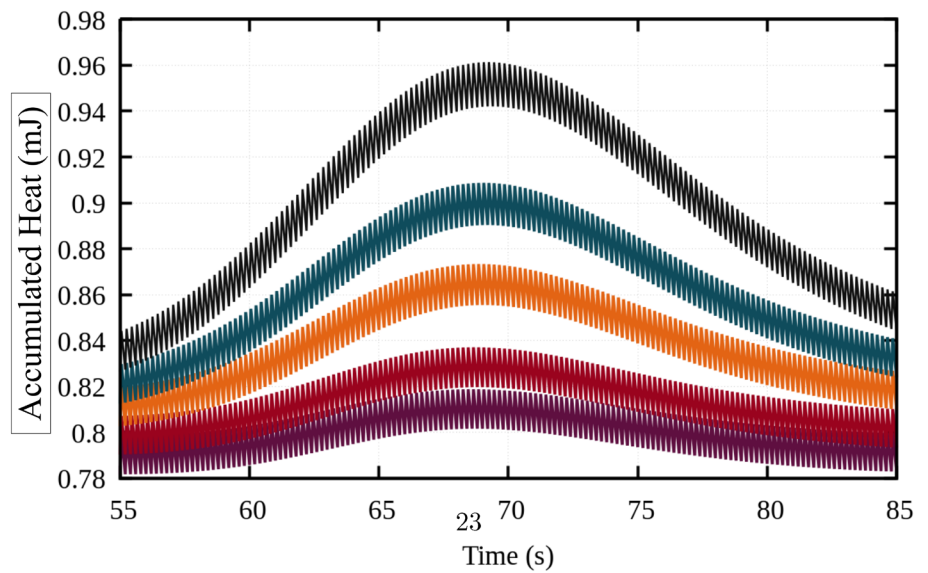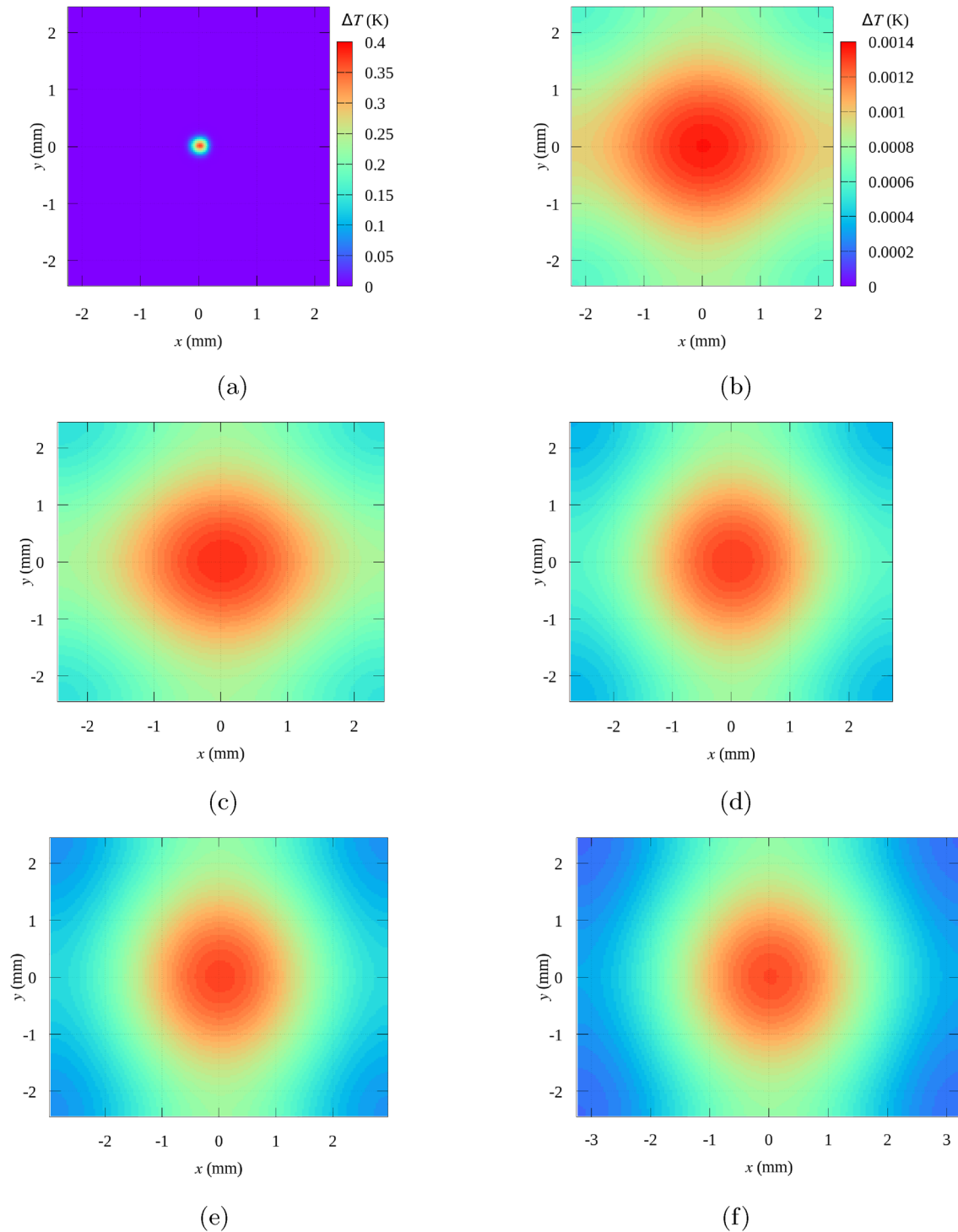
Fig. 12 Theoretical temperature distributions for samples differing in surface area to volume ratio (S_A/V). The volume (S_A/V) corresponds to the thermal distribution for the first pulse illumination. **a** Shows the sample immediately after the impact of the laser pulse, while figures. **b–f** Illustrate the heat propagation inside each sample moments before the arrival of the second pulse. It is worth noting that the sample in **b** has the smallest dimensions (4.50 mm × 4.90 mm × 2.09 mm), while **f** shows the sample with the largest dimensions (6.50 mm × 4.90 mm × 2.09 mm)
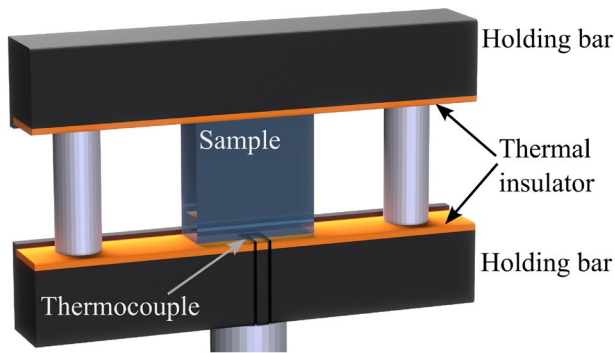
Fig. 13 Position of the sample and thermocouple during the Z-scan experiment
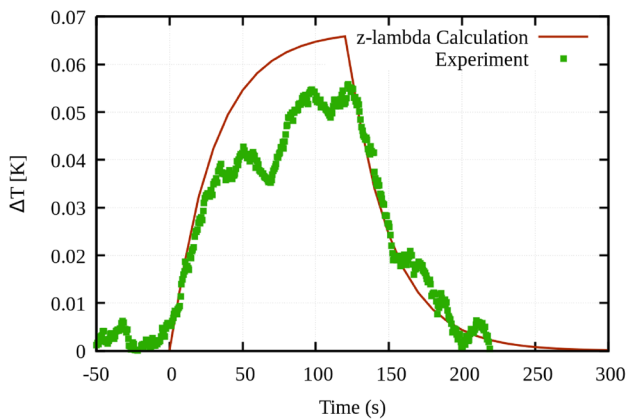

Fig. 14 The temperature of the bottom sample's surface, estimated by direct measurement (square symbol) and z-lambda theoretical calculation (solid line)
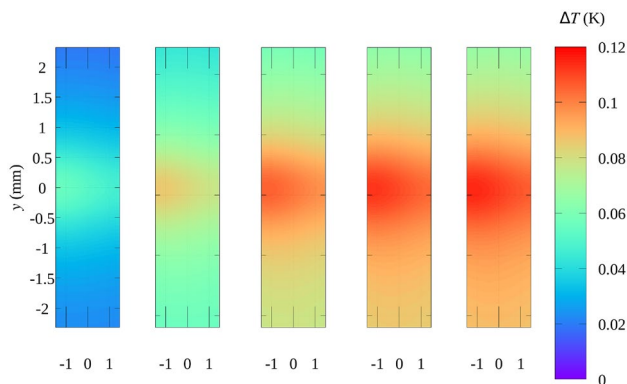

Fig. 15 Theoretical temperature distribution within $PbOGeO_2$ 2%Yb, 0.5%Tm, 1.0%Si sample at time 10 s, 30 s, 50 s, 70 s and 90 s

the lower part of the sample. Again, it is worth noting that both the upper and lower surfaces of the sample were thermally insulated, with the difference that the thermocouple is on the upper surface of the sample. The conducted tests

clearly confirm that the proposed theoretical model for determining the temperature distribution inside the sample, tested by the Z-scan method, provides correct results and presents the potential of this computational method.

4 Conclusions

The main purpose of this publication is to analyze the thermal phenomena resulting from the interaction of laser radiation with materials during a Z-scan experiment. As a result of numerical simulations, it was proved that an important factor affecting the thermal processes is not only the type of laser used and the duration of its pulse, but also the spatial geometry of the test sample. The paper quantifies how the geometry and ratio of the material under test in a Z-scan experiment affect the amount of heat received and delivered by the sample. Materials with higher S_A/V ratios heat up to higher temperatures, but absorb less heat energy from laser radiation. The temperature distribution in materials with smaller sample sizes or volumes [4 × 4 × 2] mm is more uniform compared to those with larger sample sizes [6 × 6 × 2] mm. Moreover, the results showed that the [4 × 4 × 2] mm sample achieves a higher internal temperature despite the lower thermal energy stored in it. Once again, it was confirmed that the key parameter determining the heat exchange with the environment is the ratio of the size of the surface of the material under test to its volume. In addition to these important findings, this research has contributed to the development of a new software tool. Our open source software enables precise simulations of the thermal conditions associated with Z-scan experiments, using pulsed lasers with adjustable parameters such as pulse duration, laser repetition rate, wavelength and beam profile. Moreover, it will enable researchers to accurately determine the temperature distribution in the analyzed material as a function of time. This comprehensive understanding of temperature dynamics will make it possible to assess the influence of thermal factors on the nonlinear optical parameters obtained in Z-scan experiments.

5 Glossary

Glossary and notations used in the text

Parameter	Value	Unit
Temperature equalization coefficient	$a = \lambda/(\rho \cdot c_t)$	$(\text{m}^2 \cdot \text{s}^{-1})$
Specific heat capacity	c_t	$(\text{J} \cdot \text{kg}^{-1} \cdot \text{K}^{-1})$
Electric field	E	$(\text{V} \cdot \text{m}^{-1})$
Permittivity constant in free space	ϵ_0	$(\text{F} \cdot \text{m}^{-1})$
Wave impedance	η	(Ω)
Heat transfer coefficient	h	$(\text{W} \cdot \text{m}^{-2} \cdot \text{K}^{-1})$
Electrostatic force constant	$k_0 = 1/4\pi\epsilon_0$	$(\text{N} \cdot \text{m}^2 \cdot \text{C}^{-2})$
Wave number	k_λ	(m^{-1})
Refractive index	n	(1)
Number of the nodes for numerical calculation	N_n, O_n, P_n	(1)
Time	t	(s)
Power	P	(W)
Temperature	T	(K)
Beam radius	ω	(m)
Beam waist	ω_0	(m)
Thermal conductivity	λ	$(\text{W} \cdot \text{m}^{-1} \cdot \text{K}^{-1})$
Wavelength	λ_0	(m)
Permeability of free space	μ_0	$(\text{N} \cdot \text{A}^2)$
Material density	ρ	$(\text{kg} \cdot \text{m}^{-3})$
Dimensions of the sample, height, width and length	S_H, S_W, S_L	(m)
Cartesian coordinates	x, y, z, r	(m)
Rayleigh length	z_0	(m)

Physical constants:

$\epsilon_0 = 8.854188 \times 10^{-12}$ $(\text{F} \cdot \text{m}^{-1})$

$\mu_0 = 1.256637 \times 10^{-12}$ $(\text{N} \cdot \text{A}^2)$

$k_0 = 9 \times 10^9$ $(\text{N} \cdot \text{m}^2 \cdot \text{C}^{-2})$

Author contributions R.M. and I.F-J. jointly conceptualized the study, designed the experiments, conducted numerical simulations, and analyzed the results. They equally contributed to writing the main manuscript text, including figures, and developing the z-lambda software. L.K. made essential contributions to the scientific interpretation of the results and provided language corrections for the manuscript. All authors, R.M., I.F-J., and L.K., actively participated in reviewing and editing the manuscript, ensuring the accuracy and coherence of the final document. This statement accurately reflects the contributions of each author, and we confirm that all authors have read and approved the final manuscript.

Declarations

References

1. I.A. Roberts, C.J. Wang, R. Esterlein, M. Stanford, D.J. Mynors, A three-dimensional finite element analysis of the temperature field during laser melting of metal powders in additive layer manufacturing. Int. J. Mach. Tools Manuf. **49**(12), 916–923 (2009). https://doi.org/10.1016/j.ijmachtools.2009.07.004

2. Z. Wenxiao, W. Xiang, H. Jiangbo, Z. Xuelin, Melting process and mechanics on laser sintering of single layer polyamide 6 powder. Int. J. Adv. Manuf. Technol. **69**, 901–908 (2013). https://doi.org/10.1007/s00170-013-5113-8

3. A. Foroozmehr, M. Badrossamay, E. Foroozmehr, S. Golabi, Finite element simulation of selective laser melting process considering optical penetration depth of laser in powder bed. Mater. Design **89**, 255–263 (2016). https://doi.org/10.1016/j.matdes.2015.10.002

4. A. Bonakdar, M. Molavi-Zarandi, A. Chamanfar, M. Jahazi, A. Firoozrai, E. Morin, Finite element modeling of the electron beam welding of INCONEL-713LC gas turbine blades. J. Manuf. Process. **26**, 339–354 (2017). https://doi.org/10.1016/j.jmapro.2017.02.011

5. A.V. Gusarov, I. Yadroitsev, P. Bertrand, I. Smurov, Model of radiation and heat transfer in laser-powder interaction zone at selective laser melting. J. Heat Transf. **131**(7), 072101 (2009). https://doi.org/10.1115/1.3109245. https://arxiv.org/abs/https://asmedigitalcollection.asme.org/heattransfer/article-pdf/131/7/072101/5723732/072101_1.pdf

6. L.C. Malacarne, N.G.C. Astrath, M.L. Baesso, Unified theoretical model for calculating laser-induced wavefront distortion in optical materials. J. Opt. Soc. Am. B **29**(7), 1772–1777 (2012). https://doi.org/10.1364/JOSAB.29.001772

7. J. Lee, D.H. Reitze, Analytic spatial and temporal temperature profile in a finite laser rod with input laser pulses. Opt. Express **23**(3), 2591–2599 (2015). https://doi.org/10.1364/OE.23.002591

8. J. Rousseau, E. Frangin, P. Marin, L. Daudeville, Multidomain finite and discrete elements method for impact analysis of a concrete structure. Eng. Struct. **31**, 2735–2743 (2009). https://doi.org/10.1016/j.engstruct.2009.07.001

9. H. Haddad, M. Guessasma, J. Fortin, Heat transfer by conduction using dem-fem coupling method. Comput. Mater. Sci. **81**, 339–347 (2014). https://doi.org/10.1016/j.commatsci.2013.08.033

10. M.M. Khader, A.M. Megahed, Numerical simulation using the finite difference method for the flow and heat transfer in a thin liquid film over an unsteady stretching sheet in a saturated porous medium in the presence of thermal radiation. J. King Saudi Univ. Eng. Sci. **25**(1), 29–34 (2013). https://doi.org/10.1016/j.jksues.2011.10.002

11. H.-C. Tran, Y.-L. Lo, Heat transfer simulations of selective laser melting process based on volumetric heat source with powder size consideration. J. Mater. Process. Technol. **255**, 411–425 (2018). https://doi.org/10.1016/j.jmatprotec.2017.12.024

12. L. Ladani, J. Romano, W. Brindley, S. Burlatsky, Effective liquid conductivity for improved simulation of thermal transport in laser

beam melting powder bed technology. Addit. Manuf. **14**, 13–23 (2017). https://doi.org/10.1016/j.addma.2016.12.004

13. W. Nagourney, Oxford University Press (2014). https://doi.org/10.1093/acprof:oso/9780199665488.003.0001

14. G.F. Marshall, G.E. Stutz, Taylor & Francis Group (2012). https://doi.org/10.1093/acprof:oso/9780199665488.003.0001

15. J. Goldak, A. Chakravarti, M. Bibby, A new finite element model for welding heat sources. Metall. Trans. B **15**(2), 299–305 (1984). https://doi.org/10.1007/BF02667333

16. M. Sheik-Bahae, A.A. Said, T.-H. Wei, D.J. Hagan, E.W. Van Stryland, Sensitive measurement of optical nonlinearities using a single beam. J. Quantum Electron. **26**(4), 760–769 (1990). https://doi.org/10.1109/3.53394

17. M. Sheik-Bahae, A.A. Said, T.-H. Wei, D.J. Hagan, E.W. Van Stryland, Sensitive measurement of optical nonlinearities using a single beam. IEEE J. Quantum Electron. **26**(4), 760–769 (1990). https://doi.org/10.1109/3.53394

18. M. Sheik-Bahae, A.A. Said, E.W.V. Stryland, High-sensitivity, single-beam n_2 measurements. Opt. Lett. **14**(17), 955–957 (1989). https://doi.org/10.1364/OL.14.000955

19. S. Liu, H. Zhu, G. Peng, J. Yin, X. Zeng, Microstructure prediction of selective laser melting $AlSi_{10}Mg$ using finite element analysis. Mater. Design **142**, 319–328 (2018). https://doi.org/10.1016/j.matdes.2018.01.022

20. Y. Li, D. Gu, Parametric analysis of thermal behavior during selective laser melting additive manufacturing of aluminum alloy powder. Mater. Design **63**, 856–867 (2014). https://doi.org/10.1016/j.matdes.2014.07.006

21. Y. Li, D. Gu, Thermal behavior during selective laser melting of commercially pure titanium powder: numerical simulation and experimental study. Addit. Manuf. **1–4**, 99–109 (2014). https://doi.org/10.1016/j.addma.2014.09.001

22. D. Anderson, J. Tannehill, R. Pletcher, *Computational Fluid Mechanics and Heat Transfer* (Crc Press, Boca Raton, 2014)

23. Z. Zhang, Y. Huang, A. Rani Kasinathan, S. Imani Shahabad, U. Ali, Y. Mahmoodkhani, E. Toyserkani, 3-dimensional heat transfer modeling for laser powder-bed fusion additive manufacturing with volumetric heat sources based on varied thermal conductivity and absorptivity. Opt. Laser Technol. **109**, 297–312 (2019). https://doi.org/10.1016/j.optlastec.2018.08.012

24. M. Sheik-Bahae, A.A. Said, E.W.V. Stryland, High-sensitivity, single-beam n_2 measurements. Opt. Lett. **14**(17), 955–957 (1989). https://doi.org/10.1364/OL.14.000955

25. R. Miedzinski, I. Fuks-Janczarek, Non-linear optics study of the samples which strongly diffuse the gaussian beam. Opt. Laser Technol. **115**, 193–199 (2019). https://doi.org/10.1016/j.optlastec.2019.01.042

26. R. Miedzinski, I. Fuks-Janczarek, M. Reben, Y. El Sayed Said, Z-scan measurements of the third-order optical nonlinearities and linear optical properties of $70TeO_2$–$5MxOy$–$10P_2O_5$–$10ZnO$–$5PbF_2$ glasses doped with Er^{3+} ions modified by transition metals. Opt. Mater. **85**, 48–54 (2018). https://doi.org/10.1016/j.optmat.2018.08.033

27. J. Taler, P. Duda, *Solving Direct and Inverse Heat Conduction Problems* (Springer, Berlin–Heidelberg, 2006)

28. A. Bejan, *Heat Transfer* (Wiley, New York, 1993)

29. R. Miedziński, I. Fuks-Janczarek, Z-lambda: a terminal-based software for simulation of heat transfer during z-scan experiments in transparent solids. SoftwareX **24**, 101535 (2023). https://doi.org/10.1016/j.softx.2023.101535

30. R. Miedzinski, I. Fuks-Janczarek, Z-lambda Software (2022). http://www.fizyka.ujd.edu.pl/index.php/zlambda

31. I. Fuks-Janczarek, R. Miedzinski, L.R.P. Kassab, F.M. Alves, Nonlinear optical features on Yb3+/Tm3+ codoped PBO-GEO2 glasses with Si nanoparticles. Mater. Res. Bull. **77**, 8–14 (2016). https://doi.org/10.1016/j.materresbull.2016.01.032